

# Symmetry-Indicated Time-Reversal-Doubled Axion Insulators

Yue Xie,<sup>1,2</sup> Haohao Sheng,<sup>1,2</sup> Quansheng Wu,<sup>1,3</sup> Xi Dai,<sup>4</sup>  
Zhong Fang,<sup>1,3</sup> Hongming Weng,<sup>1,3,\*</sup> and Zhijun Wang<sup>1,3,†</sup>

<sup>1</sup>*Beijing National Laboratory for Condensed Matter Physics,  
and Institute of Physics, Chinese Academy of Sciences, Beijing 100190, China*

<sup>2</sup>*University of Chinese Academy of Sciences, Beijing 100049, China*

<sup>3</sup>*Condensed Matter Physics Data Center, Chinese Academy of Sciences, Beijing 100190, China*

<sup>4</sup>*Department of Physics, Hong Kong University of Science and Technology, Hong Kong 999077, China*

(Dated: March 3, 2026)

The axion insulator exhibits a topological magnetoelectric effect characterized by an axion angle  $\theta = \pi$ , while the time-reversal-doubled axion insulator ( $T$ -DAXI) can be viewed as two copies of an axion insulator related by time-reversal symmetry. In this work, we show that a topological crystalline insulator with nonsymmorphic glide or screw symmetry hosts the  $T$ -DAXI phase. The spin-resolved topology of the  $T$ -DAXI phase is guaranteed by the nonsymmorphic symmetry invariant  $\delta_g = 1$  or  $\delta_s = 1$  in certain spin directions. In this phase, the partial axion angles are quantized to  $\pi$ , and the gapped surfaces realize half-quantized quantum spin Hall states. By applying an external magnetic field along the  $z$  direction, electrons with opposite spins accumulate on opposite (001) surfaces, producing a topological spin polarization in real space. When the magnetic field is time-periodic, this leads to an alternating spin current detectable in experiment. Using *ab initio* calculations, we demonstrate that mixed bismuth monohalides  $\text{Bi}_4\text{Br}_x\text{I}_{4-x}$  realize the nonsymmorphic  $T$ -DAXI with  $\delta_g = \delta_s = 1$ . Our findings not only reveal the symmetry-enforced  $T$ -DAXIs in nonsymmorphic topological crystalline insulators, but also introduce the spin magnetoelectric effect as a novel topological spin response.

## I. INTRODUCTION

In recent decades, topological phases of matter have attracted sustained interest in condensed matter physics and materials science [1–7]. One of the intriguing properties characteristic of three-dimensional (3D) topological materials is the topological magnetoelectric effect arising from an effective action  $S_\theta = \frac{\theta e^2}{4\pi^2} \int dt d^3\mathbf{x} \mathbf{E} \cdot \mathbf{B}$ , where  $\theta$  is the axion angle defined over a period of  $2\pi$  [8–12]. An insulator with  $\theta = \pi$  quantized by symmetry that reverses odd times of space-time coordinates (*e.g.*  $I$ ,  $T\tau$ ,  $M$ ,  $C_2T$ ) is termed a (magnetic) axion insulator (AXI), and exhibits a detectable quantized magnetoelectric response [13–16]. The AXI can be constructed from weakly coupled Chern-insulator layers, where two layers in each unit cell carry opposite Chern number  $C = \pm 1$  and are alternately stacked along the  $z$  direction [17–19]. Materials such as  $\text{MnBi}_2\text{Te}_4$  [20–23],  $\text{Eu}_3\text{In}_2\text{As}_4$  [24] and others [25–33] have been theoretically proposed as candidates for AXIs. Moreover, an AXI features half of a quantum anomalous Hall (QAH) state on a surface due to the parity anomaly [34–36]. In fact, the half-quantized surface conductivity is carried by the chiral hinge states [37], which links AXIs to chiral higher-order topological insulators (HOTIs), or magnetic topological crystalline insulators (TCIs) [17, 38–45].

On the other hand, time-reversal ( $T$ -) invariant TCIs [46–52] host gapless helical boundary states at ter-

minations that preserve protecting crystalline symmetries [53, 54]. An example is the helical hinge states in  $T$ -invariant inversion TCIs with inversion index  $Z_4 = 2$  [55–59], also known as helical HOTIs [60–62]. Recent work [63] has shown that for a chosen spin-resolved direction, an inversion TCI can realize three refined spin-resolved topological phases: a 3D quantum spin Hall insulator (QSHI), a spin Weyl-fermion state, and notably a  $T$ -invariant doubled axion insulator ( $T$ -DAXI). The  $T$ -DAXI can be viewed as two copies of a magnetic AXI related by time-reversal symmetry, with partial axion angles quantized by inversion symmetry. However, both 0 and  $\pi$  of the partial axion angles are allowed in an inversion TCI, depending on the details of the projected spin bands. These facts raise several natural questions: (i) can  $T$ -DAXI phases arise with partial axion angles quantized by other crystalline symmetries, such as glides or magnetic screws; (ii) can a  $T$ -DAXI be guaranteed in a TCI, with partial axion angles enforced to be  $\pi$ ; (iii) what is the spin analogue of the topological axion response?

In this work, we introduce the spin-resolved topological classifications for 3D  $T$ -invariant nonsymmorphic TCIs with glide  $g_y \equiv \{M_y | 0, 0, 0.5\}$  or screw  $s_2 \equiv \{C_{2z} | 0, 0, 0.5\}$  symmetry. In the  $s_y$  ( $s_{xy}$ ) spin-resolved topology, we find that the  $T$ -DAXI phases are guaranteed/enforced by the nonsymmorphic symmetry, where the partial axion angle defined in a spin subspace is quantized by the symmetry  $g_y$  ( $s_2T$ ). To illustrate the properties of the nonsymmorphic  $T$ -DAXI, we construct a glide TCI model as an example and reveal the following properties, including the quantized partial axion angles  $\theta^\pm = \pi$ , surface quantum anomalies with a surface half-quantized spin Chern number plateau  $-C_{s,\text{top}} = C_{s,\text{bot}} =$

\* hmweng@iphy.ac.cn

† wzj@iphy.ac.cn

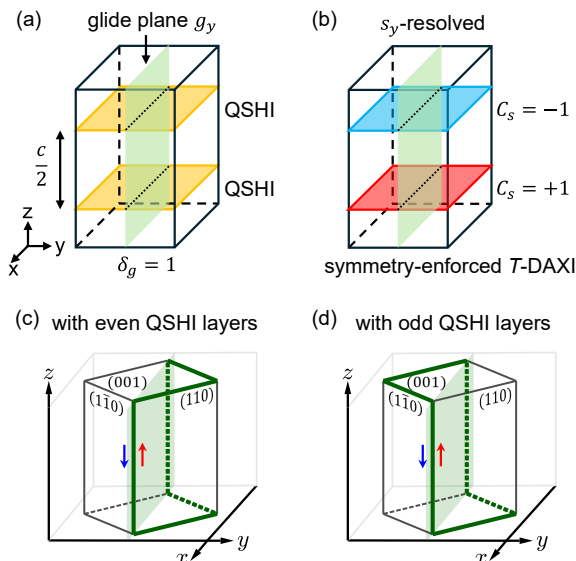


FIG. 1. (Color online) (a) A  $T$ -invariant gTCI in the layer construction scenario, where two glide-related QSHIs are stacked in the  $z$ -direction. (b) Spin-resolved topology in the  $s_y$  spin direction for a gTCI of (a). The two QSHIs carry opposite spin Chern numbers due to the glide symmetry. The system therefore realizes a  $T$ -DAXI with partial axion angles quantized by glide. (c) Schematic plots of the helical hinge states (dark green lines) for a gTCI in a prismatic geometry, with an even number of QSHI layers. The hinge states on the top and bottom surfaces lie on the same side of the glide plane (light-green plane). (d) Hinge-state configuration with an odd number of QSHI layers, obtained by removing the top-most QSHI layer. The hinge states on the top surface shift to the opposite side. In both cases, the helical hinge states propagate around the entire sample.

$1/2$ , and a topological spin magnetoelectric response that produces a detectable transport signature. Finally, using *ab initio* calculations, we predict that the mixed bismuth monohalides  $\text{Bi}_4\text{BrI}_3$  and  $\text{Bi}_4\text{Br}_3\text{I}$  can realize the nonsymmorphic  $T$ -DAXI phase, providing a promising platform for experimental detection.

## II. $T$ -DAXIS IN NONSYMMORPHIC TCIS

To investigate the spin-resolved topology, one has to separate the occupied-band space into two spin subspaces by projecting the spin operator  $\hat{s}_n$  [64],

$$\begin{aligned} S_n(\mathbf{k}) &= P(\mathbf{k})\hat{s}_n P(\mathbf{k}), \\ S_n |\psi_{m\mathbf{k}}^\pm\rangle &= \lambda_{m\mathbf{k}}^\pm |\psi_{m\mathbf{k}}^\pm\rangle, \end{aligned} \quad (1)$$

where  $P(\mathbf{k}) = \sum_{m \in \text{occ}} |\psi_{m\mathbf{k}}\rangle \langle \psi_{m\mathbf{k}}|$  projects onto the occupied-band space, and  $n$  denotes the spin direction. Since a gap generally exists between upper and lower spin bands, labeled by eigenvalues  $\lambda_{m\mathbf{k}}^+$  and  $\lambda_{m\mathbf{k}}^-$ , the occupied bands can be separated into two sectors. Thus in a QSHI,

one can define partial Chern numbers  $C^\pm$  for the two sectors, with time-reversal symmetry requiring  $C^+ = -C^-$ . Accordingly, the spin Chern number  $C_s \equiv (C^+ - C^-)/2$  is interpreted as the topological contribution to the intrinsic spin Hall conductivity (SHC),  $\sigma_s = C_s \frac{e}{2\pi}$  [65, 66].

A glide TCI (gTCI) can be constructed in real space by stacking QSHI layers in the  $z$  direction, where two QSHIs per unit cell are related by  $g_y$  and individually occupy the  $(000; d_0)$  and  $(000; d_0 + \frac{c}{2})$  planes [here  $(hkl; d)$  denotes Miller indices  $hkl$  and the distance  $d$  to the origin], as shown in Fig. 1(a). A screw TCI (sTCI) is constructed by simply replacing the glide plane with a two-fold screw axis. Such layer constructions yield a glide/screw invariant  $\delta_{g/s} = 1$  with trivial strong and weak time-reversal  $\mathbb{Z}_2$  indices  $(\nu_0; \nu_1 \nu_2 \nu_3) = (0; 000)$  for the gTCIs/sTCIs [55], which we refer to as nonsymmorphic TCIs in this work. For a gTCI, when the bands are separated by the eigenvalues of  $P s_y P$ , the  $g_y$  symmetry is preserved in each spin sector and can quantize the partial axion angle. Based on spin-resolved bubble equivalence analysis, the spin-resolved topology is  $\mathbb{Z}_2$ -classified. In Fig. 1(b), since the two QSHIs are related by  $g_y$ , the  $s_y$  spin Chern numbers of them are opposite, consistent with a nontrivial partial axion angle  $\theta^\pm = \pi$  in both spin sectors. Therefore, the system realizes the spin-resolved topological state of a  $T$ -DAXI. For other spin-resolved directions, the  $T$ -DAXI phase is not allowed/protected because the partial axion angles are no longer quantized due to the lack of  $g_y$  in each set of spin bands. Additionally, when the bands are separated by  $s_{xz}$  (we denote  $s_{xz}$  for an arbitrary direction in the  $xz$  plane), the partial Chern numbers for each QSHI layer are identical due to  $g_y T$ , and the spin-resolved topology is  $\mathbb{Z}$ -classified, corresponding to a spin-resolved 3D QSHI. Regarding an sTCI with  $s_2$  symmetry, the spin-resolved topology for spin directions in the  $xy$  plane yields  $T$ -DAXIs, whose partial axion angles are quantized by  $s_2 T$  symmetry, while the  $s_z$  spin resolution produces an  $s_2$ -protected 3D QSHI. In particular, unlike in inversion-symmetric TCIs [63], the  $T$ -DAXIs in gTCIs (sTCIs) are guaranteed by the nonsymmorphic symmetries in the  $s_y$  ( $s_{xy}$ ) spin resolution.

## III. MINIMAL MODEL

To study the  $T$ -DAXI in nonsymmorphic TCI, we take gTCI as an example and construct an eight-band model,

$$\begin{aligned} H_g(\mathbf{k}) &= \begin{pmatrix} H_+(k_x, k_y) & H_1(k_z) \\ H_1^\dagger(k_z) & H_-(k_x, k_y) \end{pmatrix}, \\ H_\pm(k_x, k_y) &= M_k s_0 \sigma_z + v_x \sin k_x s_z \sigma_x - v_y \sin k_y s_0 \sigma_y \\ &\quad \pm A_x \sin k_x s_y \sigma_x \pm A_y \sin k_y s_x \sigma_x, \\ M_k &= m + t \cos k_x + t \cos k_y, \\ H_1(k_z) &= e^{i \frac{k_z}{2}} \left( f_1 \cos \frac{k_z}{2} + f_2 \sin \frac{k_z}{2} \right). \end{aligned} \quad (2)$$

TABLE I. Spin-resolved topological classifications in spinful 3D nonsymmorphic TCIs.  $\theta^+$  is the partial axion angle and  $C^+$  is the partial Chern number in the upper spin subspace. Due to the time reversal symmetry,  $\theta^+ = \theta^-$  and  $C^+ = -C^-$ .

Nonsymmorphic TCI	$g_y = \{M_y   0, 0, 0.5\}$		$s_2 = \{C_{2z}   0, 0, 0.5\}$		
	Spin direction	$y$ axis	$xz$ plane	$xy$ plane	$z$ axis
Symmetry in a subspace	$g_y$	$g_y T$	$s_2 T$	$s_2$	$s_2$
Topological number	$\theta^\pm$	$C^\pm$	$\theta^\pm$	$C^\pm$	$C^\pm$
Classification and topology	$\mathbb{Z}_2$ ( $T$ -DAXI)	$\mathbb{Z}$ (3D QSHI)	$\mathbb{Z}_2$ ( $T$ -DAXI)	$\mathbb{Z}$ (3D QSHI)	$\mathbb{Z}$ (3D QSHI)

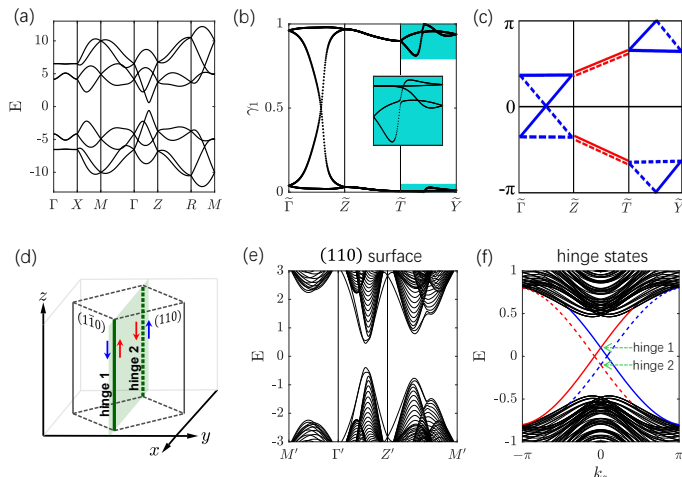


FIG. 2. (Color online) (a) Bulk energy bands of the gTCI model in Eq. (2). The parameters are  $-m = t = 2$ ,  $v_x = v_y = A_x = A_y = 2$ ,  $t_1 = t_4 = 0.5$ ,  $t_5 = t_2 = 2$  and  $t_6 = -t_3 = 1.5$ . (b) WCCs  $\gamma_1$  of the  $k_x$ -directed Wilson loop for the four occupied bands. The zigzag pattern of hourglass Wilson bands characteristic of the gTCI phase is clearly observed. (c) Adapted from Ref. [67]: schematic illustration of the Wilson loop for a gTCI with hourglass-type connection. (d) Schematic plot of a rod geometry used in (f), where the  $(1\bar{1}0)$  and  $(110)$  directions are open while the  $(001)$  direction is periodic. (e) Gapped surface energy bands of the  $(110)$  surface, which are the same as those of the  $(1\bar{1}0)$  surface due to  $g_y$ . (f) Energy bands for the rod geometry shown in (d). The helical hinge states localized at the interface of the  $(110)$  and  $(1\bar{1}0)$  surfaces are clearly visible.

Here,  $\tau$ ,  $s$  and  $\sigma$  are Pauli matrices for layer, spin and orbital degrees of freedom, respectively.  $H_+$  and  $H_-$  describe the two QSHI layers (with  $|m| < |2t|$ ) in a unit cell, respectively located at  $(001; d_0)$  and  $(001; d_0 + \frac{c}{2})$ , and related by the glide symmetry  $g_y$ . We choose  $d_0 = 0$  and  $c = 1$  without loss of generality.  $H_1(k_z)$  represents the interlayer coupling with  $f_1 = t_1 s_0 \sigma_0 + it_2 s_y \sigma_x + it_3 s_x \sigma_0$  and  $f_2 = it_4 s_0 \sigma_x + t_5 s_y \sigma_0 + t_6 s_x \sigma_x$ . The energy bands of the gTCI model  $H_g(\mathbf{k})$  are shown in Fig. 2(a).

If  $H_1(k_z)$  is omitted, based on the real-space layer construction, the model realizes a gTCI with invariants  $\delta_g = 1$  and  $(\nu_0; \nu_1 \nu_2 \nu_3) = (0; 000)$  [55]. Upon adding  $H_1(k_z)$  without closing the bulk gap, these invariants remain unchanged. In addition, the gTCI can also be confirmed by the zigzag pattern of hourglass Wilson bands

on a glide-preserving surface. To illustrate this, we compute the  $k_x$ -directed Wilson loop and plot the Wannier charge centers (WCCs) along the  $(100)$ -surface Brillouin-zone path  $\tilde{\Gamma}\tilde{Z}\tilde{T}\tilde{Y}$  in Fig. 2(b). One can see that the Wilson bands have the nontrivial zigzag pattern, which is identical to Fig. 2(c) adapted from Ref. [67], confirming a  $\delta_g = 1$  gTCI. Therefore, the spin-resolved topology in the  $s_y$  direction yields a  $T$ -DAXI as discussed above.

On glide-preserved surfaces, the hourglass-like surface states are expected in a gTCI. However, on the  $(110)$  surface without glide symmetry, a glide-breaking perturbation introduces a mass term that gaps the surface spectrum. Meanwhile, due to the glide symmetry, the  $(1\bar{1}0)$  surface has the same spectrum, but with an opposite-signed mass term. Consequently, helical hinge states emerge at the interface between the two surfaces. We calculate the hinge-state energy bands for a rod geometry (along the  $z$  direction), bounded by the  $(110)$  and  $(1\bar{1}0)$  surfaces, as shown in Fig. 2(f). The presence of the topological helical hinge states demonstrates that a glide TCI also manifests itself as a helical HOTI. We further find that the helical hinge states extend to encircle the entire sample of a nonsymmorphic TCI, and the position of the hinge states is related to the number of total QSHI layers, as schematically plotted in Fig. 1(c,d).

#### IV. PROPERTIES OF A $T$ -DAXI

In this section, we study the properties of the  $T$ -DAXI in the  $s_y$ -resolved topology of our gTCI model in three aspects, including partial axion angles, surface partial quantum anomalies, and spin magnetoelectric response.

##### A. Partial axion angles

As viewed as two  $T$ -related copies of a magnetic AXI, the  $T$ -DAXI can be characterized by partial axion angles  $\theta^\pm$ , which can be evaluated from partial Wannier functions constructed in terms of the spin-subspace Bloch wavefunctions [18]. In this scenario, for an  $L$ -unit-cell slab along the  $z$  direction, we define an auxiliary slab partial axion term,

$$\theta_{slabL}^\pm = -\frac{1}{L} \int d^2\mathbf{k} \sum_{n=1}^L \left[ z_{n\mathbf{k}}^\pm \tilde{\Omega}_{\mathbf{k}n}^{xy,\pm} \right], \quad (3)$$

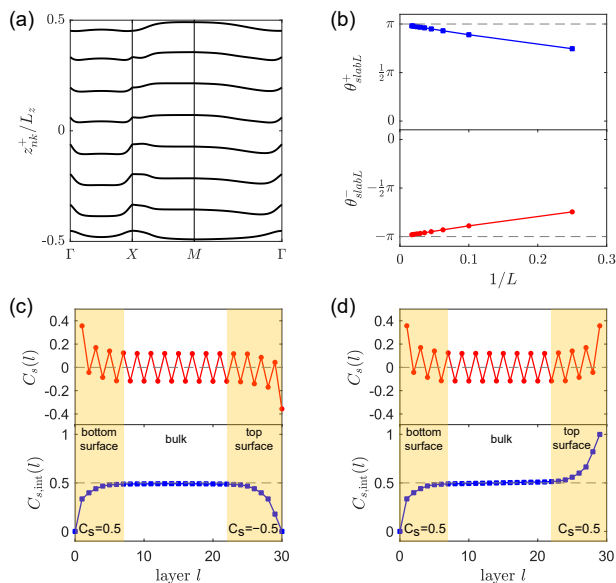


FIG. 3. (Color online) (a) Partial WCCs  $z_{n\mathbf{k}}^+$  for the  $s_y$  upper spin bands of a 4-unit slab, where 8 upper spin Wannier bands are located on 8 layers (two QSHI layers per unit cell). (b) Evolution of the slab partial axion terms  $\theta_{slabL}^\pm$  in the  $s_y$  resolution as a function of  $1/L$ .  $\theta_{slabL}^\pm$  are quantized to  $\pm\pi$  as  $L \rightarrow \infty$ , indicating a  $T$ -DAXI phase. (c) Upper panel: layer-dependent spin Chern number  $C_s(l)$  for a 15-unit-cell slab.  $C_s(l)$  is mainly confined to the surfaces and oscillates around zero in the bulk. Lower panel: accumulated spin Chern number  $C_{s,int}(l)$  up to depth  $l$ , which yields a vanishing total spin Chern number but exhibits a clear half-quantized plateau, with half-quantized spin Chern number  $C_{s,bot} = -C_{s,top} = 1/2$  on the bottom and top surfaces (yellow shaded regions). (d) Layer-dependent spin Chern number and its accumulation for a modified slab after removing the topmost QSHI layer. The half-quantized plateau persists, while the sign of  $C_{s,top}$  flips. The total spin Chern number thus becomes  $C_s = 1$ .

where  $z_{n\mathbf{k}}^\pm$  are the partial WCCs along the  $z$ -direction defined in the spin subspaces, and  $\tilde{\Omega}_{kn}^{xy,\pm}$  is the associated partial non-Abelian Berry curvature [68–71]. In the infinite thickness limit, the slab partial axion terms in Eq. (3) converge to the partial axion angles defined by the Chern-Simons three-form [18] in the two spin subspaces, *i.e.*,  $\theta^\pm = \lim_{L \rightarrow \infty} \theta_{slabL}^\pm$ .

For illustration, in the  $s_y$  resolution, we show  $z_{n\mathbf{k}}^+$  for the upper spin bands of a 4-unit-cell slab of our gTCI model in Fig. 3(a). Eight separated partial WCCs correspond to the eight weakly coupled QSHI layers. In Fig. 3(b), the upper (lower) panel shows the evolution of  $\theta_{slabL}^+$  ( $\theta_{slabL}^-$ ) as a function of the inverse of  $L$ . The intercepts on the  $y$  axis indicate  $\theta^\pm = \pm\pi$ , confirming the  $T$ -DAXI phase. Here, the signs “ $\pm$ ” before  $\pi$  are still well defined by means of the asymptotic convergence behavior together with time-reversal symmetry.

## B. Layer-dependent spin Chern numbers

We now discuss the surface anomaly implied by the partial axion angles. In a magnetic AXI, the surface AHC is half-quantized as  $\sigma^{\text{AHC}} = \frac{e^2}{2h}$  [10, 13, 34, 35]. Regarding a  $T$ -DAXI, the net surface AHC vanishes because of the time-reversal symmetry. However, the topological contribution to the surface SHC should be non-trivial and half-quantized as  $\sigma^{\text{SHC}} = \frac{e}{4\pi}$  [63]. This half-quantized surface SHC feature can be captured using the layer-dependent spin Chern number  $C_s(l) = \frac{1}{2} [C^+(l) - C^-(l)]$ , where  $C^\pm(l)$  resolve the TKNN integer into contributions from individual layers [13],

$$C^\pm(l) = \frac{i}{2\pi} \int d^2k \text{Tr} [P_{\mathbf{k}}^\pm \epsilon_{ij} (\partial_i P_{\mathbf{k}}^\pm) P_l (\partial_j P_{\mathbf{k}}^\pm)]. \quad (4)$$

Here,  $\epsilon_{ij}$  is the antisymmetric tensor with  $i, j \in \{k_x, k_y\}$ .  $P_{\mathbf{k}}^\pm = \sum_n |\psi_{n\mathbf{k}}^\pm\rangle \langle \psi_{n\mathbf{k}}^\pm|$  project onto the two spin subspaces, and  $P_l$  projects onto the  $l$ -th layer of a slab ( $l \in [1, 2L]$ ). In the upper panel of Fig. 3(c), we plot the layer-dependent spin Chern number in the  $s_y$  resolution for an  $L$ -unit-cell slab of the gTCI model.  $C_s(l)$  is primarily localized on the surfaces and decays to zero in the bulk in an oscillatory manner. We then accumulate the layer-dependent spin Chern number to depth  $l$  according to  $C_{s,int}(l) = \sum_{l'=1}^l \bar{C}_s(l')$ , with  $\bar{C}_s(l') = \frac{1}{2} [C_s(l') + C_s(l'+1)]$  being the average of two neighboring layers [34]. The results are plotted in the lower panel of Fig. 3(c). Although the total spin Chern number of the slab vanishes, the spin Chern numbers on the bottom and top surfaces are half-quantized to  $C_{s,bot} = -C_{s,top} = 1/2$ , consistent with the surface partial quantum anomaly of a  $T$ -DAXI. Moreover, if we modify the slab by removing the topmost QSHI layer (a half unit cell) from the slab (resulting in  $l \in [1, 2L - 1]$ ), the half-quantized plateau on the remaining surfaces persists while the sign of  $C_{s,top}$  flips (*i.e.*,  $C_{s,top} = 1/2$ ). And consequently, the total spin Chern number of the modified slab becomes nonzero,  $C_s = 1$ .

## C. Spin magnetoelectric response

For a magnetic AXI, the quantized axion angle  $\theta = \pi$  implies a topological magnetoelectric response: an applied magnetic field  $B$  induces a quantized charge polarization  $\mathbf{P} = e^2 \mathbf{B} / 2h$  parallel to the magnetic field, so that electrons accumulate on one surface from the opposite surface [8, 9] [see Fig. 4(a)]. In a  $T$ -DAXI, the net charge response vanishes because of time-reversal symmetry, but the partial axion angles imply that electrons carrying opposite spins will accumulate on two opposite surfaces, producing a spin polarization parallel to the external magnetic field, as shown in Fig. 4(b).

To calculate the real-space spin polarization in the gTCI model with parameters modified to  $s_y$  conservation, we consider an  $L$ -unit-cell slab under a static magnetic field  $\mathbf{B} = (0, 0, B)$  applied along the  $z$  direction,

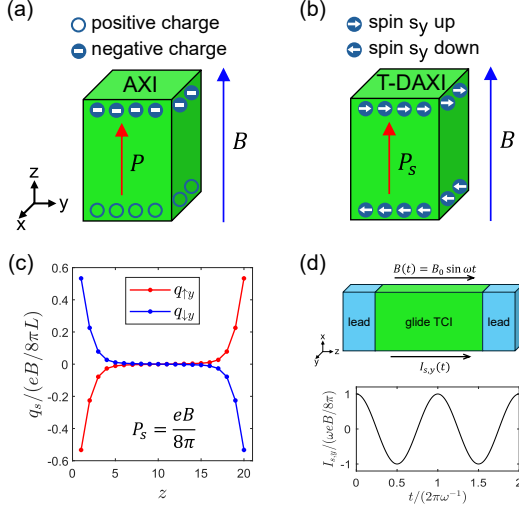


FIG. 4. (Color online) (a) Topological charge polarization induced by an external magnetic field in a magnetic AXI. (b) Topological spin polarization induced by an external magnetic field in a  $T$ -DAXI. (c) For  $s_y$ -conserved parameters by setting  $v_x = A_y = t_3 = t_6 = 0$  and  $t_1 = t_4 = 1.5$ , the  $s_y$  spin distributions in each unit cell are shown along the  $z$  direction under a  $z$ -directed magnetic field. Red and blue dotted lines indicate  $s_y$  up and  $s_y$  down, respectively. The total spin polarization reaches the quantized value  $P_s = eB/8\pi$ . (d) AC spin current in a gTCI tunneling junction induced by a time-periodic external magnetic field.

which contributes the Peierls substitution  $e \frac{2\pi i e}{h} \int dt \cdot \mathbf{A}$  with  $\mathbf{A} = (-yB, 0, 0)$ . We obtain the  $s_y$  spin distribution via  $q_s(z) = \frac{\hbar}{2V} \langle \hat{N}_s(z) \rangle$ , where  $\hat{N}_s(z)$  with  $s = \uparrow_y$  and  $\downarrow_y$  are the total-density operators at position  $z$  for spin up and spin down of  $s_y$ , respectively.  $V$  is the volume of the slab. In Fig. 4(c), we show the  $s_y$  spin distributions along the  $z$  direction  $q_s(z)$  for a 20-unit-cell slab, measured relative to an average  $\bar{q}_s = \sum_z q_s(z)/L$ . One clearly sees that  $s_y$ -up electrons transfer from the bottom surface to the top surface while  $s_y$ -down electrons transfer in the opposite direction, producing a real-space spin polarization. We further quantify the spin polarization by  $P_s = \sum_z z[q_{\uparrow y}(z) - q_{\downarrow y}(z)]$  and it quantizes to  $P_s = eB/8\pi$ , determined by the partial axion angles. Moreover, if the applied magnetic field is time-periodic with a frequency  $\omega$ ,  $B(t) = B_0 \sin \omega t$ , the spin polarization should also be periodic and thus generate an alternating spin current with  $I_s = \frac{dP_s(t)}{dt} = \omega e B_0 \cos(\omega t)/8\pi$  in a tunneling junction. This provides a direct transport signature of the spin magnetoelectric response in a  $T$ -DAXI.

## V. APPLICATION TO $\text{Bi}_4\text{Br}_x\text{I}_{4-x}$

The mixed bismuth monohalides  $\text{Bi}_4\text{Br}_x\text{I}_{4-x}$  ( $x = 1, 3$ ) have been synthesized experimentally [72], which crystallize in a base-centered structure belonging to the space

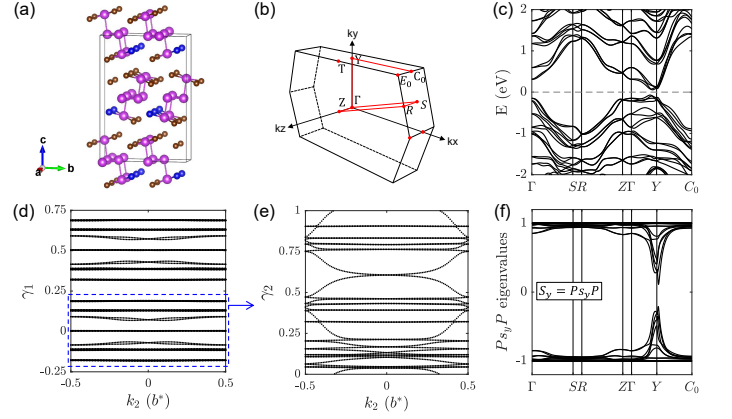


FIG. 5. (Color online) (a) Crystal structure of  $\text{Bi}_4\text{Br}_3\text{I}$ . (b) Bulk Brillouin zone. (c) Electronic band structure (including SOC). (d)  $k_z$ -directed Wilson loop. (e)  $k_1$ -directed nested Wilson loop  $\gamma_2$  for the WCCs around  $\gamma_1 = 0$  inside the blue frame, which shows a helical winding pattern. The WCCs around  $\gamma_1 = 0.5$  should show the same nested Wilson loop pattern due to  $g_y$  or  $s_2$ . These form a QSHI layer construction on the  $(001; 0)$  and  $(001; \frac{\pi}{2})$  planes, indicating a nonsymmorphic TCI with  $\delta_g = \delta_s = 1$  and  $(\nu_0; \nu_1\nu_2\nu_3) = (0; 000)$ . (f) Spin bands formed by eigenvalues of  $S_y(\mathbf{k})$ , where a spin-band gap is clearly observed.

group  $Cmc2_1$ . We take  $\text{Bi}_4\text{Br}_3\text{I}$  of Fig. 5(a) as an example in the main text. The chains extend along the  $a$  axis and assemble into layers within the  $ab$  plane. Two adjacent van der Waals (vdW) layers form an AB stacking arrangement and are related by both glide  $g_y$  and screw  $s_2$  symmetries, while an interlayer sliding breaks the inversion symmetry of the bulk crystal. The electronic band structure of  $\text{Bi}_4\text{Br}_3\text{I}$  including SOC is plotted in Fig. 5(c), showing a global bulk gap. Due to the time-reversal symmetry, it can be classified by four  $\mathbb{Z}_2$  topological invariants. A Wilson loop calculation yields  $(\nu_0; \nu_1\nu_2\nu_3) = (0; 000)$ , indicating that the compound is neither a strong nor a weak 3D TI. Nevertheless, in Fig. 5(d), we show WCCs  $\gamma_1$  of the  $k_z$ -directed Wilson loop. Two sets of isolated WCCs are located around  $\gamma_1 = 0$  and  $\gamma_1 = 0.5$ . Fig. 5(e) further shows the  $k_1$ -directed nested Wilson loop for the WCCs around  $\gamma_1 = 0$  (inside the blue frame). A nontrivial winding pattern indicates a  $\mathbb{Z}_2 = 1$  QSHI layer at  $(001; 0)$  plane. Due to  $g_y$  and  $s_2$ , another QSHI layer is located at  $(001; \frac{\pi}{2})$ . By real-space layer construction, this reveals a nonsymmorphic TCI protected by both  $g_y$  and  $s_2$ . In short, our calculations show that  $\text{Bi}_4\text{Br}_3\text{I}$  is a nonsymmorphic TCI with  $\delta_g = \delta_s = 1$  and  $(\nu_0; \nu_1\nu_2\nu_3) = (0; 000)$ . Therefore, in the  $s_y$  spin direction,  $\text{Bi}_4\text{Br}_3\text{I}$  is guaranteed to realize a  $T$ -DAXI phase. To further verify the spin-resolved topology, we have performed the spin-resolved nested Wilson loop calculations, whose results agree with the spin-resolved topological classification in nonsymmorphic TCIs discussed in Section II. In addition, a new bulk phase of  $\text{Bi}_4\text{Br}_4$  and  $\text{Bi}_4\text{I}_4$ —denoted as the  $\gamma$  phase—is

theoretically predicted to be dynamically stable [73] and also realizes  $T$ -DAXI in our calculations.

## VI. CONCLUSION AND DISCUSSION

In summary, we have identified spin-resolved topological classifications in nonsymmorphic TCIs. Particularly, in certain spin-resolved directions, the  $T$ -DAXI is guaranteed by nonsymmorphic symmetries. Explicitly, the  $g_y/s_2T$ -protected  $T$ -DAXI is indicated by the glide/screw invariant  $\delta_{g/s} = 1$  with trivial time-reversal  $\mathbb{Z}_2$  indices  $(\nu_0; \nu_1\nu_2\nu_3) = (0; 000)$ . Nonsymmorphic TCIs that realize  $T$ -DAXIs also exhibit helical hinge states that surround the whole sample, resembling higher-order topological insulators. Moreover, the  $T$ -DAXI is revealed to be characterized by several spin-resolved features: quantized partial axion angles, half-quantized surface spin Chern numbers, and topological spin polarizations. Some novel experimentally accessible signatures of the  $T$ -DAXI can then be proposed. (i) The glide/screw-protected helical hinge states encircling the entire sample provide a spectroscopic signature accessible to angle-resolved photoemission spectroscopy or scanning tunneling microscopy. (ii) The surface quantum anomaly produces opposite, topologically contributed half-quantized spin Hall conductivities  $-\sigma_{\text{top}}^{s,y} = \sigma_{\text{bot}}^{s,y} = e/4\pi$  on the top and bottom surfaces, which can be probed in a spin-transport experiment. (iii) Due to the spin magnetoelectric response, a time-periodic external magnetic field

can generate an alternating spin current in a tunnel junction, providing a dynamical transport probe of the partial axion physics. These experiments can be performed in the mixed bismuth monohalides  $\text{Bi}_4\text{Br}_x\text{I}_{4-x}$  and in other TCIs with nonsymmorphic symmetries. Furthermore, by changing the slab sample between even and odd layer counts, the total spin Chern number of a gTCI/sTCI can be controlled to vanish or quantize to 1, and the response of the system accordingly alternates between a  $T$ -DAXI and a QSHI. This layer sensitivity suggests a route towards layer-manipulated “layertronics”. In addition, although this work focuses on  $T$ -invariant systems, the symmetry arguments should naturally generalize to magnetic gTCIs and sTCIs. In those magnetic nonsymmorphic TCIs, one can expect that chiral hinge states appear surrounding the whole samples, and that the axion angles are quantized to  $\pi$  by the nonsymmorphic symmetries, with quantized magnetoelectric responses measurable without involving gapless boundary states. Finally, we anticipate that this work will motivate further experimental and theoretical studies on material realizations and device concepts that exploit partial axion physics.

## ACKNOWLEDGMENTS

This work was supported by the National Natural Science Foundation of China (Grant No. 12188101), the National Key R&D Program of China (Grant No. 2022YFA1403800), and the Center for Materials Genome.

- 
- [1] M. Z. Hasan and C. L. Kane, Colloquium: Topological insulators, *Rev. Mod. Phys.* **82**, 3045 (2010).
  - [2] X.-L. Qi and S.-C. Zhang, Topological insulators and superconductors, *Rev. Mod. Phys.* **83**, 1057 (2011).
  - [3] C. L. Kane and E. J. Mele, Quantum spin hall effect in graphene, *Phys. Rev. Lett.* **95**, 226801 (2005).
  - [4] B. A. Bernevig, T. L. Hughes, and S.-C. Zhang, Quantum spin hall effect and topological phase transition in hgte quantum wells, *Science* **314**, 1757 (2006).
  - [5] C. L. Kane and E. J. Mele, Quantum spin hall effect in graphene, *Phys. Rev. Lett.* **95**, 226801 (2005).
  - [6] C. L. Kane and E. J. Mele,  $Z_2$  topological order and the quantum spin hall effect, *Phys. Rev. Lett.* **95**, 146802 (2005).
  - [7] L. Fu, C. L. Kane, and E. J. Mele, Topological insulators in three dimensions, *Phys. Rev. Lett.* **98**, 106803 (2007).
  - [8] X.-L. Qi, T. L. Hughes, and S.-C. Zhang, Topological field theory of time-reversal invariant insulators, *Phys. Rev. B* **78**, 195424 (2008).
  - [9] R. Li, J. Wang, X.-L. Qi, and S.-C. Zhang, Dynamical axion field in topological magnetic insulators, *Nature Physics* **6**, 284 (2010).
  - [10] F. Wilczek, Two applications of axion electrodynamics, *Phys. Rev. Lett.* **58**, 1799 (1987).
  - [11] A. Sekine and K. Nomura, Axion electrodynamics in topological materials, *Journal of Applied Physics* **129**, 141101 (2021).
  - [12] D. M. Nenko, C. A. C. Garcia, J. Gooth, C. Felser, and P. Narang, Axion physics in condensed-matter systems, *Nature Reviews Physics* **2**, 682 (2020).
  - [13] A. M. Essin, J. E. Moore, and D. Vanderbilt, Magnetoelectric polarizability and axion electrodynamics in crystalline insulators, *Phys. Rev. Lett.* **102**, 146805 (2009).
  - [14] N. Pournaghavi, A. Pertsova, A. H. MacDonald, and C. M. Canali, Nonlocal sidewall response and deviation from exact quantization of the topological magnetoelectric effect in axion-insulator thin films, *Phys. Rev. B* **104**, L201102 (2021).
  - [15] Y.-H. Li and R. Cheng, Identifying axion insulator by quantized magnetoelectric effect in antiferromagnetic  $\text{MnBi}_2\text{Te}_4$  tunnel junction, *Phys. Rev. Res.* **4**, L022067 (2022).
  - [16] Y. Wan, J. Li, and Q. Liu, Topological magnetoelectric response in ferromagnetic axion insulators, *National Science Review* **11**, nwac138 (2022).
  - [17] L. Elcoro, B. J. Wieder, Z. Song, Y. Xu, B. Bradlyn, and B. A. Bernevig, Magnetic topological quantum chemistry, *Nature Communications* **12**, 5965 (2021).

- [18] N. Varnava, I. Souza, and D. Vanderbilt, Axion coupling in the hybrid wannier representation, *Phys. Rev. B* **101**, 155130 (2020).
- [19] Z.-D. Song, B. Lian, R. Queiroz, R. Ilan, B. A. Bernevig, and A. Stern, Delocalization transition of a disordered axion insulator, *Phys. Rev. Lett.* **127**, 016602 (2021).
- [20] D. Zhang, M. Shi, T. Zhu, D. Xing, H. Zhang, and J. Wang, Topological axion states in the magnetic insulator  $\text{MnBi}_2\text{Te}_4$  with the quantized magnetoelectric effect, *Phys. Rev. Lett.* **122**, 206401 (2019).
- [21] J. Li, Y. Li, S. Du, Z. Wang, B.-L. Gu, S.-C. Zhang, K. He, W. Duan, and Y. Xu, Intrinsic magnetic topological insulators in van der waals layered  $\text{mnbi}_2\text{te}_4$ -family materials, *Science Advances* **5**, eaaw5685 (2019).
- [22] Y. Gong, J. Guo, J. Li, K. Zhu, M. Liao, X. Liu, Q. Zhang, L. Gu, L. Tang, X. Feng, D. Zhang, W. Li, C. Song, L. Wang, P. Yu, X. Chen, Y. Wang, H. Yao, W. Duan, Y. Xu, S.-C. Zhang, X. Ma, Q.-K. Xue, and K. He, Experimental realization of an intrinsic magnetic topological insulator, *Chin. Phys. Lett.* **36**, 076801 (2019).
- [23] C. Liu, Y. Wang, H. Li, Y. Wu, Y. Li, J. Li, K. He, Y. Xu, J. Zhang, and Y. Wang, Robust axion insulator and chern insulator phases in a two-dimensional antiferromagnetic topological insulator, *Nature Materials* **19**, 522 (2020).
- [24] J. Yao, R. Zhang, S. Zhang, H. Sheng, Y. Shi, Z. Fang, H. Weng, and Z. Wang, Axion insulator, weyl points, quantum anomalous hall effect, and magnetic topological phase transition in  $\text{eu}_3\text{in}_2\text{as}_4$ , *Phys. Rev. B* **111**, L041117 (2025).
- [25] J. Gooth, B. Bradlyn, S. Honnali, C. Schindler, N. Kumar, J. Noky, Y. Qi, C. Shekhar, Y. Sun, Z. Wang, B. A. Bernevig, and C. Felser, Axionic charge-density wave in the weyl semimetal  $(\text{tase}_4)_2\text{i}$ , *Nature* **575**, 315 (2019).
- [26] G. M. Pierantozzi, A. D. Vita, C. Bigi, X. Gui, H.-J. Tien, D. Mondal, F. Mazzola, J. Fujii, I. Vobornik, G. Vinai, A. Sala, C. Africh, T.-L. Lee, G. Rossi, T.-R. Chang, W. Xie, R. J. Cava, and G. Panaccione, Evidence of magnetism-induced topological protection in the axion insulator candidate  $\text{eusn}_2\text{p}_2$ , *Proceedings of the National Academy of Sciences* **119**, e2116575119 (2022).
- [27] X. Gui, I. Pletikosić, H. Cao, H.-J. Tien, X. Xu, R. Zhong, G. Wang, T.-R. Chang, S. Jia, T. Valla, W. Xie, and R. J. Cava, A new magnetic topological quantum material candidate by design, *ACS Central Science* **5**, 900 (2019).
- [28] Y. Xu, Z. Song, Z. Wang, H. Weng, and X. Dai, Higher-order topology of the axion insulator  $\text{euin}_2\text{as}_2$ , *Phys. Rev. Lett.* **122**, 256402 (2019).
- [29] N. Varnava and D. Vanderbilt, Surfaces of axion insulators, *Phys. Rev. B* **98**, 245117 (2018).
- [30] M. Mogi, M. Kawamura, R. Yoshimi, A. Tsukazaki, Y. Kozuka, N. Shirakawa, K. S. Takahashi, M. Kawasaki, and Y. Tokura, A magnetic heterostructure of topological insulators as a candidate for an axion insulator, *Nature Materials* **16**, 516 (2017).
- [31] M. Mogi, M. Kawamura, A. Tsukazaki, R. Yoshimi, K. S. Takahashi, M. Kawasaki, and Y. Tokura, Tailoring tricolor structure of magnetic topological insulator for robust axion insulator, *Science Advances* **3**, eaao1669 (2017).
- [32] R. S. K. Mong, A. M. Essin, and J. E. Moore, Antiferromagnetic topological insulators, *Phys. Rev. B* **81**, 245209 (2010).
- [33] R. A. Müller, N. R. Lee-Hone, L. Lapointe, D. H. Ryan, T. Pereg-Barnea, A. D. Bianchi, Y. Mozharivskiy, and R. Flacau, Magnetic structure of  $\text{gdbipt}$ : A candidate antiferromagnetic topological insulator, *Phys. Rev. B* **90**, 041109 (2014).
- [34] N. Varnava and D. Vanderbilt, Surfaces of axion insulators, *Phys. Rev. B* **98**, 245117 (2018).
- [35] T. Olsen, M. Taherinejad, D. Vanderbilt, and I. Souza, Surface theorem for the chern-simons axion coupling, *Phys. Rev. B* **95**, 075137 (2017).
- [36] H. Zhou, H. Li, D.-H. Xu, C.-Z. Chen, Q.-F. Sun, and X. C. Xie, Transport theory of half-quantized hall conductance in a semimagnetic topological insulator, *Phys. Rev. Lett.* **129**, 096601 (2022).
- [37] M. Gong, H. Liu, H. Jiang, C.-Z. Chen, and X.-C. Xie, Half-quantized helical hinge currents in axion insulators, *National Science Review* **10**, nwad025 (2023).
- [38] W. A. Benalcazar, B. A. Bernevig, and T. L. Hughes, Quantized electric multipole insulators, *Science* **357**, 61 (2017).
- [39] W. A. Benalcazar, B. A. Bernevig, and T. L. Hughes, Electric multipole moments, topological multipole moment pumping, and chiral hinge states in crystalline insulators, *Phys. Rev. B* **96**, 245115 (2017).
- [40] J. Langbehn, Y. Peng, L. Trifunovic, F. von Oppen, and P. W. Brouwer, Reflection-symmetric second-order topological insulators and superconductors, *Phys. Rev. Lett.* **119**, 246401 (2017).
- [41] Z. Song, Z. Fang, and C. Fang,  $(d-2)$ -dimensional edge states of rotation symmetry protected topological states, *Phys. Rev. Lett.* **119**, 246402 (2017).
- [42] F. Schindler, A. M. Cook, M. G. Vergniory, Z. Wang, S. S. P. Parkin, B. A. Bernevig, and T. Neupert, Higher-order topological insulators, *Science Advances* **4**, eaat0346 (2018).
- [43] M. Ezawa, Magnetic second-order topological insulators and semimetals, *Phys. Rev. B* **97**, 155305 (2018).
- [44] Y. Xu, L. Elcoro, Z.-D. Song, B. J. Wieder, M. G. Vergniory, N. Regnault, Y. Chen, C. Felser, and B. A. Bernevig, High-throughput calculations of magnetic topological materials, *Nature* **586**, 702 (2020).
- [45] J. Gao, Z. Guo, H. Weng, and Z. Wang, Magnetic band representations, fu-kane-like symmetry indicators, and magnetic topological materials, *Phys. Rev. B* **106**, 035150 (2022).
- [46] L. Fu, Topological crystalline insulators, *Phys. Rev. Lett.* **106**, 106802 (2011).
- [47] T. H. Hsieh, H. Lin, J. Liu, W. Duan, A. Bansil, and L. Fu, Topological crystalline insulators in the snite material class, *Nature Communications* **3**, 982 (2012).
- [48] Z. Wang, A. Alexandradinata, R. J. Cava, and B. A. Bernevig, Hourglass fermions, *Nature* **532**, 189194 (2016).
- [49] C. Fang and L. Fu, New classes of topological crystalline insulators having surface rotation anomaly, *Science Advances* **5**, eaat2374 (2019).
- [50] M. G. Vergniory, L. Elcoro, C. Felser, N. Regnault, B. A. Bernevig, and Z. Wang, A complete catalogue of high-quality topological materials, *Nature* **566**, 480 (2019).
- [51] T. Zhang, Y. Jiang, Z. Song, H. Huang, Y. He, Z. Fang, H. Weng, and C. Fang, Catalogue of topological electronic materials, *Nature* **566**, 475 (2019).
- [52] F. Tang, H. C. Po, A. Vishwanath, and X. Wan, Comprehensive search for topological materials using symmetry

- indicators, *Nature* **566**, 486 (2019).
- [53] B. J. Wieder and B. A. Bernevig, *The axion insulator as a pump of fragile topology* (2018), [arXiv:1810.02373](https://arxiv.org/abs/1810.02373).
- [54] F. Schindler, S. S. Tsirkin, T. Neupert, B. Andrei Bernevig, and B. J. Wieder, Topological zero-dimensional defect and flux states in three-dimensional insulators, *Nature Communications* **13**, 5791 (2022).
- [55] Z. Song, T. Zhang, Z. Fang, and C. Fang, Quantitative mappings between symmetry and topology in solids, *Nature Communications* **9**, 3530 (2018).
- [56] E. Khalaf, H. C. Po, A. Vishwanath, and H. Watanabe, Symmetry indicators and anomalous surface states of topological crystalline insulators, *Phys. Rev. X* **8**, 031070 (2018).
- [57] H. C. Po, A. Vishwanath, and H. Watanabe, Symmetry-based indicators of band topology in the 230 space groups, *Nature Communications* **8**, 50 (2017).
- [58] E. Khalaf, Higher-order topological insulators and superconductors protected by inversion symmetry, *Phys. Rev. B* **97**, 205136 (2018).
- [59] Z. Wang, B. J. Wieder, J. Li, B. Yan, and B. A. Bernevig, Higher-order topology, monopole nodal lines, and the origin of large fermi arcs in transition metal dichalcogenides  $x\text{Te}_2$  ( $x = \text{Mo}, \text{W}$ ), *Phys. Rev. Lett.* **123**, 186401 (2019).
- [60] F. Schindler, A. M. Cook, M. G. Vergniory, Z. Wang, S. S. P. Parkin, B. A. Bernevig, and T. Neupert, Higher-order topological insulators, *Science Advances* **4**, eaat0346 (2018).
- [61] J. Langbehn, Y. Peng, L. Trifunovic, F. von Oppen, and P. W. Brouwer, Reflection-symmetric second-order topological insulators and superconductors, *Phys. Rev. Lett.* **119**, 246401 (2017).
- [62] Z. Song, Z. Fang, and C. Fang,  $(d-2)$ -dimensional edge states of rotation symmetry protected topological states, *Phys. Rev. Lett.* **119**, 246402 (2017).
- [63] K.-S. Lin, G. Palumbo, Z. Guo, Y. Hwang, J. Blackburn, D. P. Shoemaker, F. Mahmood, Z. Wang, G. A. Fiete, B. J. Wieder, and B. Bradlyn, Spin-resolved topology and partial axion angles in three-dimensional insulators, *Nature Communications* **15**, 550 (2024).
- [64] E. Prodan, Robustness of the spin-chern number, *Phys. Rev. B* **80**, 125327 (2009).
- [65] D. N. Sheng, Z. Y. Weng, L. Sheng, and F. D. M. Haldane, Quantum spin-hall effect and topologically invariant chern numbers, *Phys. Rev. Lett.* **97**, 036808 (2006).
- [66] D. Monaco and L. Ulčakar, Spin hall conductivity in insulators with nonconserved spin, *Phys. Rev. B* **102**, 125138 (2020).
- [67] A. Alexandradinata, Z. Wang, and B. A. Bernevig, Topological insulators from group cohomology, *Phys. Rev. X* **6**, 021008 (2016).
- [68] M. Taherinejad and D. Vanderbilt, Adiabatic pumping of chern-simons axion coupling, *Phys. Rev. Lett.* **114**, 096401 (2015).
- [69] N. Marzari and D. Vanderbilt, Maximally localized generalized wannier functions for composite energy bands, *Phys. Rev. B* **56**, 12847 (1997).
- [70] X. Wu, O. Diéguez, K. M. Rabe, and D. Vanderbilt, Wannier-based definition of layer polarizations in perovskite superlattices, *Phys. Rev. Lett.* **97**, 107602 (2006).
- [71] D. Ceresoli, T. Thonhauser, D. Vanderbilt, and R. Resta, Orbital magnetization in crystalline solids: Multi-band insulators, chern insulators, and metals, *Phys. Rev. B* **74**, 024408 (2006).
- [72] E. V. Dikarev, B. A. Popovkin, and A. V. Shevelkov, New polymolecular bismuth monohalides: Synthesis and crystal structures of  $\text{Bi}_4\text{Br}_x\text{I}_{4-x}$  ( $x = 1, 2, \text{ or } 3$ ), *Russian Chemical Bulletin* **50**, 2304 (2001).
- [73] H. Sheng *et al.*, Three-dimensional topological ferroelectrics, In preparation.